THE JOURNAL OF PHYSICAL CHEMISTRY C
A JOURNAL OF THE AMERICAN CHEMICAL SOCIETY

pubs.acs.org/JPCC

Article

Low-Pressure Induced Disproportionation of Barium Distannide

Amanda H. Trout, Kelsey L. Hodge, Michael Scudder, Joshua E. Goldberger, and David W. McComb*

Cite This: J. Phys. Chem. C 2021, 125, 15496−15502

Read Online

ACCESS | Metrics & More | Article Recommendations | Supporting Information

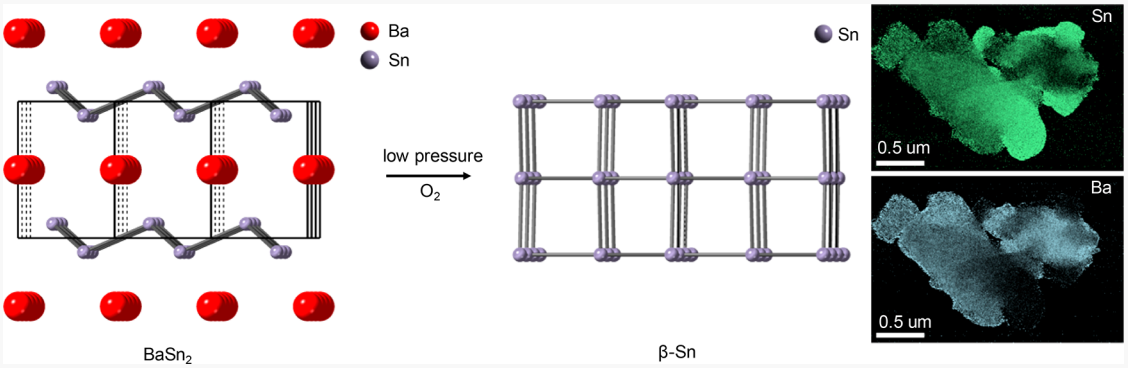

ABSTRACT: Barium distannide ($BaSn_2$), a potential precursor for stannene, is predicted to be a topological insulator. However, little is known about $BaSn_2$ as the material is extremely air-sensitive. Here we present, for the first time, characterization of $BaSn_2$ by scanning/transmission electron microscopy. We use advanced imaging and spectroscopy techniques to show disproportionation of $BaSn_2$ particles into β-Sn + Ba_xSn_y. X-ray diffraction analysis confirms that this disproportionation is driven by exposure to a low-pressure environment.

INTRODUCTION

Two-dimensional (2D) and layered materials have been a major topic of interest for the past two decades. As new 2D materials are discovered, the breadth of their possible applications widens. More recently there has been significant research interest in Xene materials such as silicene,[1] germanene,[2] and stanene[3,4] due to the potential of a wide array of exotic topological phenomena in these materials.[5,6] These topological phases can be synthesized through the deintercalation of a layered precursor.[7−9] One such precursor is barium distannide ($BaSn_2$), a layered Zintl phase material consisting of alternating layers of Ba^{2+} and a buckled sp^3-hybridized network of Sn. $BaSn_2$ is predicted to be a topological insulator with a 200 meV gap in the bulk and metallic surface states.[9−12] The first reported synthesis of $BaSn_2$ was in 2008;[13] however, since then very little experimental work has been done as it is extremely air-sensitive making characterization challenging.[9]

One technique capable of characterizing air-sensitive materials is scanning/transmission electron microscopy (S/TEM). With the right equipment, air-sensitive materials can be synthesized and transferred into the vacuum atmosphere of the microscope without air exposure. This allows for analysis of the as-synthesized material through atomic resolution imaging as well as spectroscopic techniques such as energy dispersive X-ray spectroscopy (EDS) and electron energy-loss spectroscopy (EELS). We present, to the best of our knowledge, the first characterization of $BaSn_2$ via S/TEM including high-resolution TEM (HRTEM) imaging, high-angle annular dark field (HAADF) STEM imaging, selected area electron diffraction (SAED), EDS, and EELS. These characterization experiments have revealed a highly unusual observation of low-pressure induced disproportionation of $BaSn_2$ into β-Sn and a Ba-rich (Ba_xSn_y) phase. Previous experiments suggest that $BaSn_2$ is a line compound; however, only partial Ba:Sn phase diagrams have been reported, and these do not include any low-temperature or low-pressure information.[14,15] Our findings suggest that $BaSn_2$ is unstable at low pressures and provide additional insight into the Ba:Sn system.

METHODS

The synthesis of $BaSn_2$ has been accomplished via a sealed fused silica tube reaction by heating up stoichiometric quantities of barium and tin to 747 °C and holding at that temperature for 10 h. The reaction is then quenched and reheated to 500 °C over 4 h and held for 100 h where it is quenched again. XRD measurements were performed on a

Received: March 12, 2021
Revised: June 28, 2021
Published: July 13, 2021

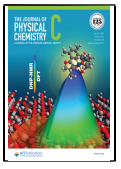

https://doi.org/10.1021/acs.jpcc.1c02246
J. Phys. Chem. C 2021, 125, 15496−15502

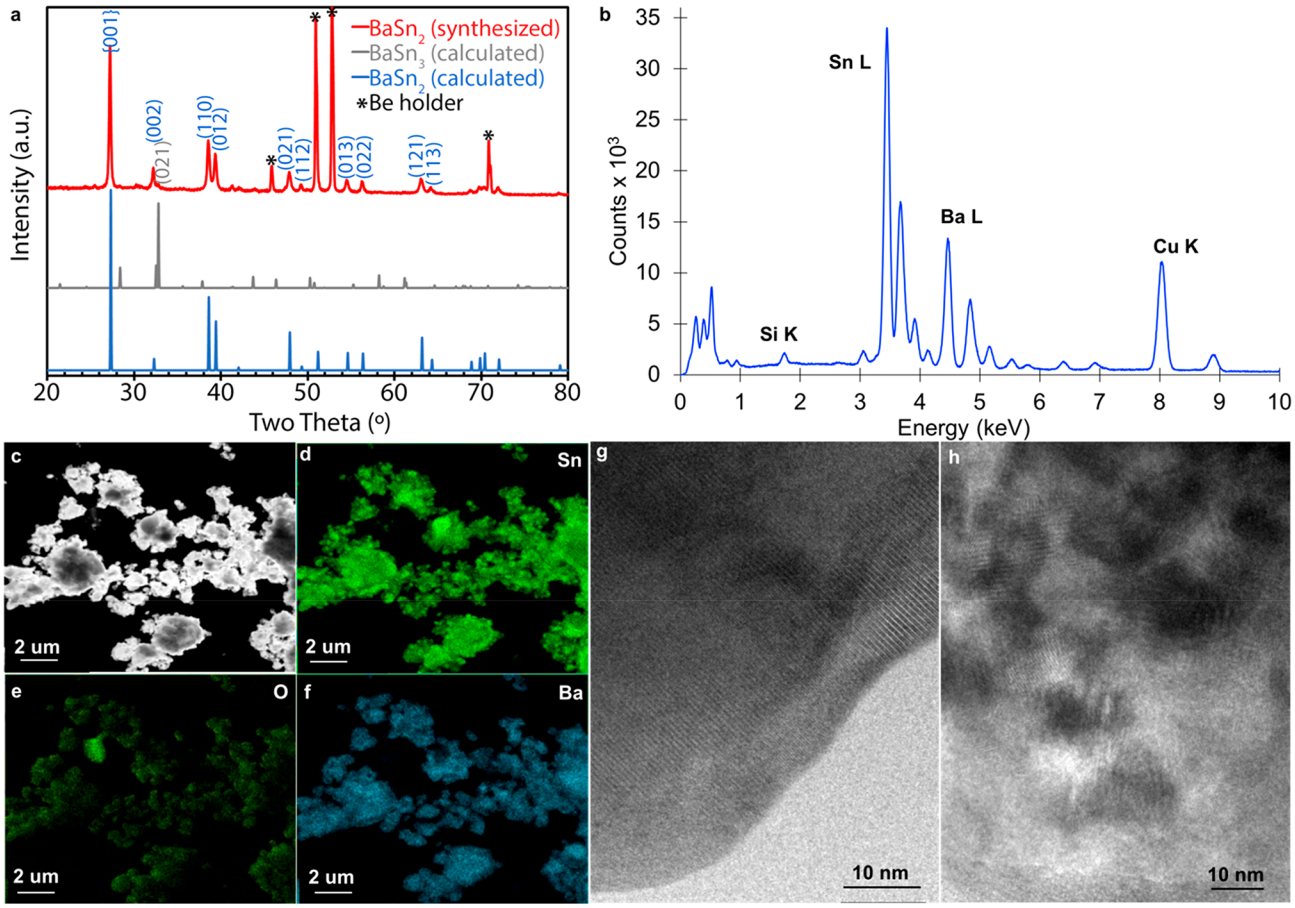

Figure 1. (a) Powder XRD of as-synthesized $BaSn_2$ (red) indicating $BaSn_2$ as the primary phase. Peaks of the main phase $BaSn_2$ are indicated in blue, and the minor side phase $BaSn_3$ peaks are indicated in gray. (b) EDS plot collected from all of the particles shown in the HAADF image (c) showing an overall Ba:Sn ratio of ~1:2. (d–f) Ba, Sn, and O elemental maps of the region from (c). HRTEM images indicate the presence of long-range ordering (g) and amorphous/polycrystalline regions (h) in individual particles.

Rigaku Miniflex using a sample holder with a beryllium window due to the extreme air sensitivity.

Following an initial powder XRD scan in an air-free Be holder, the $BaSn_2$ powder sample was loaded into the Lakeshore probe station antechamber within a N_2-filled glovebox. Kapton tape was used to secure the $BaSn_2$ sample container inside the antechamber prior to vacuum exposure. The sealed antechamber was then pumped out of the glovebox and immediately attached to the probe station and exposed to a vacuum of 10^{-4} mbar at ambient temperature. The sample of $BaSn_2$ was left under these conditions for a total of 18 h. The antechamber containing the sample powder was then detached from the probe station and pumped back into a N_2-filled glovebox. The $BaSn_2$ sample was removed, and a second XRD scan in an air-free Be sample holder was run (Figure 7).

TEM grids were prepared in a N_2-filled glovebox by cracking open $BaSn_2$ tubes and grinding 1–2 large crystals into a fine powder using a mortar and pestle. A lacey-C Cu grid was then rubbed over the ground material. The prepared grids were submerged in a vial of liquid nitrogen and transported to the microscopy facility. The grids were then removed from the liquid nitrogen and loaded into the microscope as quickly as possible. After a Gatan vacuum transfer holder was acquired, the prepared TEM grids were loaded into the holder while in the glovebox. The holder allows for transportation into the microscope while maintaining the glovebox environment.

High-resolution TEM images and selected area electron diffraction patterns were collected on a FEI Tecnai F20 S/TEM operating at 200 kV with a 70 μm objective aperture and either a 10 or 20 μm selected area aperture. EDS was performed on both a FEI Tecnai F20 operating at 200 kV and a FEI image corrected Titan3 G2 60–300 kV operating at 300 kV. The Tecnai is equipped with an EDAX TEAM silicon drift detector, and the Titan3 is equipped with a Bruker 4D quad SuperX detector. Electron energy-loss spectroscopy was collected on a FEI image corrected Titan3 G2 60–300 kV S/TEM operating at 300 kV and equipped with a Gatan Quantum spectrometer. Dual EELS spectrum images were collected with a convergence semiangle of 5.54 mrad and a collection semiangle of 10.71 mrad. The exposure times were 0.0001 s for the low-loss region and 0.2–0.3 s for the high-loss. The dispersion was 0.25 eV/channel. Low-loss data processing included removal of the zero-loss peak (ZLP) using the reflected tail method and deconvolution using the Fourier-log method in DigitalMicrograph.[16,18] High-loss data processing included a power law background subtraction before each edge of interest and deconvolution using the Fourier-ratio method.[16,18]

RESULTS AND DISCUSSION

$BaSn_2$ was synthesized from the elements using a standard sealed fused silica tube approach.[9] Following synthesis, the structure and purity of the $BaSn_2$ were confirmed via powder

https://doi.org/10.1021/acs.jpcc.1c02246
J. Phys. Chem. C 2021, 125, 15496–15502

X-ray diffraction patterns. The XRD plot in Figure 1a shows $BaSn_2$ as the primary phase with a trigonal crystal structure of space group $P\bar{3}m13$. Trace amounts of $BaSn_3$ are also present. Initially, electron microscopy was performed on this sample using TEM grids prepared in a glovebox and then frozen in liquid nitrogen in the glovebox before being transported to the electron microscope facility in liquid nitrogen, quickly loaded into the TEM grid holder, and inserted into the microscope, as described in the experimental section. Figure 1b–h shows initial TEM characterization results. When the average signal from multiple particles is analyzed, the EDS spectrum and elemental maps (Figure 1b, d–f) exhibit an average Ba:Sn ratio of 1:2, as expected, with trace amounts of oxygen observed. The oxygen is likely due to the brief time (~2–3 min) the $BaSn_2$ grid was exposed to air while the TEM grids were loaded into the holder and inserted into the microscope after removal from the liquid nitrogen. The trace amount of oxygen observed indicates that the novel liquid nitrogen transfer process is rather effective for handling air-sensitive TEM samples.

The average 1:2 ratio of Ba:Sn is not representative of the microstructure. Analysis of individual particles by EDS reveals drastic changes in stoichiometry within the particles resulting in Ba and Sn-rich regions. Additionally, HRTEM images collected on the edges of the particles show the presence of both long-range ordering and amorphous/polycrystalline material, indicating variations in the crystallinity within each particle (Figure 1g and h). The range of stoichiometries and crystallinity was not detected in XRD data collected from the same material before exposure to liquid nitrogen. Therefore, to test whether these variations are due to the liquid nitrogen transportation, we performed XRD analysis of $BaSn_2$ particles before and after exposure to liquid N_2. Additional peaks corresponding to the formation of β-Sn are observed in the post liquid N_2 data of $BaSn_2$ powder directly submerged in liquid N_2. A powder XRD pattern was also collected on $BaSn_2$ powder in a fused silica tube that was submerged in liquid N_2; however, this data does not show the presence of β-Sn (Figure 2), suggesting that low temperature is not a driving force for $BaSn_2$ disproportionation into β-Sn + Ba_xSn_y. The appearance of β-Sn in the XRD data of $BaSn_2$ directly submerged in liquid N_2 is likely due to trace amounts of H_2O in liquid N_2.

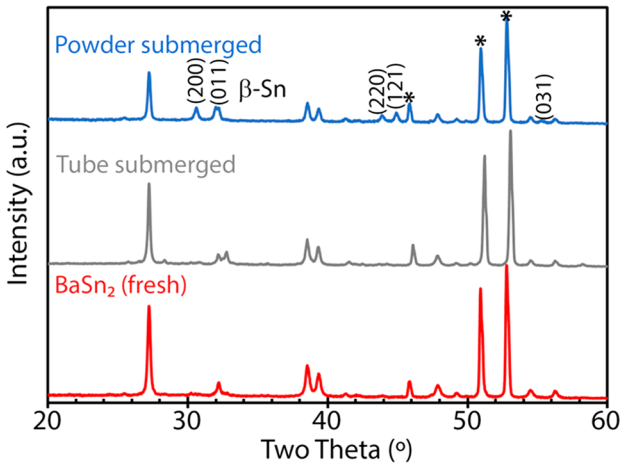

Figure 2. Powder XRD of $BaSn_2$ before (red) and after submersion of a fused silica tube into liquid nitrogen (gray) and submersion of $BaSn_2$ powder directly into liquid nitrogen (blue). The emergence of β-Sn peaks in the submerged powder is indicated (black text). Peaks from the berylium sample holder are indicated by *.

After a dedicated environmental transfer TEM specimen rod designed for air-free transportation without the use of liquid N_2 was obtained, the S/TEM characterization experiments were repeated. Despite the elimination of liquid N_2 exposure, individual particles still exhibited regions that are Sn-rich and other regions with widely varying Ba/Sn stoichiometries as shown in the EDS maps in Figure 3. STEM high-angle annular dark field (HAADF) images, EDS elemental maps, and selected area electron diffraction (SAED) patterns were used to identify correlations between the morphology, composition, and crystallinity of the varying regions within the $BaSn_2$ particles.

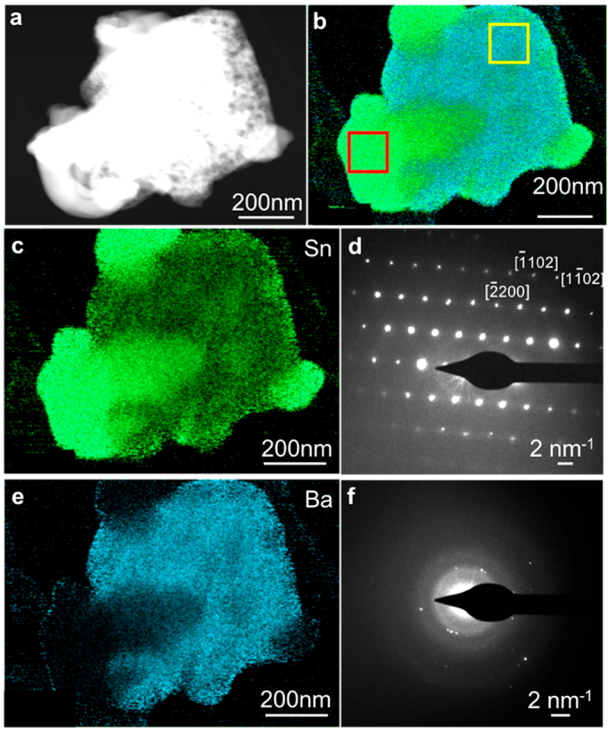

Figure 3. (a) HAADF image of a $BaSn_2$ particle showing regions with smooth morphology and others that are porous. (b, c, e) EDS maps indicating the presence of Sn (c) and Ba (e) rich regions. (d, f) SAED patterns taken from the red and yellow boxes in (b).

The red box in Figure 3b corresponds to a Sn-rich region with a Ba:Sn ratio of 1:11. Figure 3d shows the SAED pattern taken from this area which indicates the presence of long-range crystallographic order. Additionally, the diffraction pattern matches that of β-Sn viewed along [110]. In the HAADF image in Figure 3a, it is noted that this Sn-rich region exhibits rather uniform contrast which is consistent with the SAED pattern. The yellow box in Figure 3b corresponds to a Ba-rich region with a Ba:Sn ratio of 1:0.5. The SAED pattern (Figure 3f) shows that this area is primarily amorphous, and the contrast in the HAADF image has a mottled appearance that is consistent with a porous, inhomogeneous morphology. It should be emphasized that while the areas indicated by the red and yellow boxes show Sn and Ba-rich regions respectively, when the whole particle is analyzed via EDS, a Ba:Sn ratio of 1:2 is observed. These results clearly demonstrate disproportionation of $BaSn_2$ into β-Sn + Ba_xSn_y, but in this case they are observed without the exposure of the material to low

https://doi.org/10.1021/acs.jpcc.1c02246
J. Phys. Chem. C 2021, 125, 15496–15502

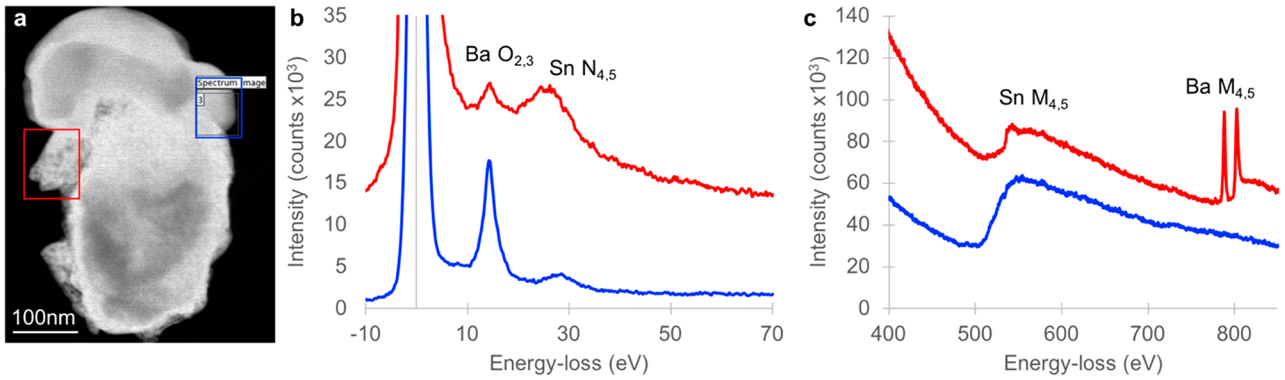

Figure 4. (a) HAADF image of a $BaSn_2$ particle with the blue box indicating the Sn region used to collect the blue low-loss (b) and high-loss (c) spectra. The red spectra in (b) and (c) indicate the presence of both Ba and Sn and were collected from the red box in (a).

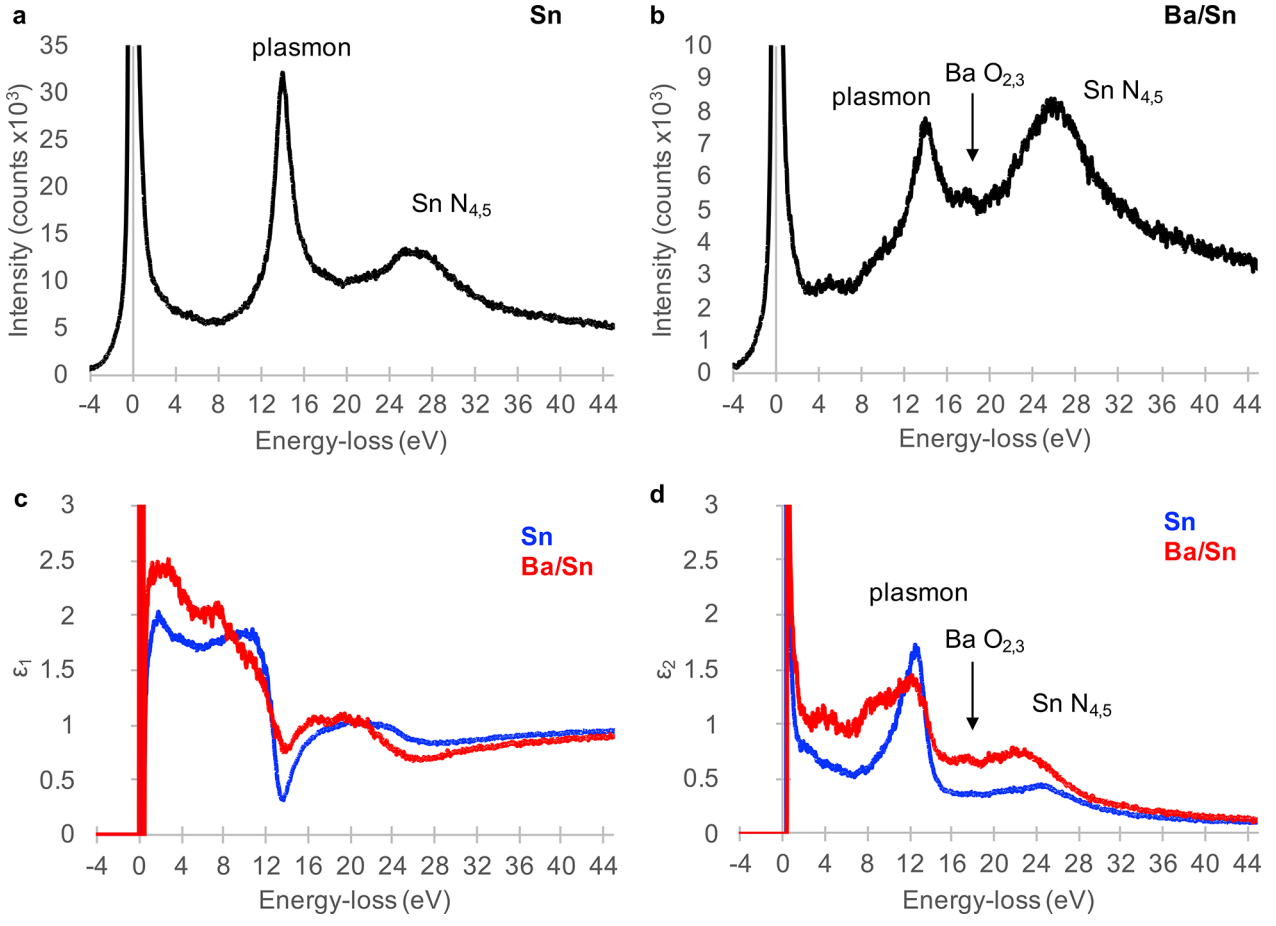

Figure 5. Raw low-loss data of Sn (a) and Ba/Sn (b) regions collected from the blue and red boxes in Figure 4. Comparison of ε_1 (c) and ε_2 (d) after Kramers−Kronig analysis of the Sn (blue) and Ba/Sn (red) regions.

temperatures, suggesting that disproportionation occurs due to an alternative driving force.

S/TEM electron energy-loss spectroscopy (EELS) can also be used for compositional analysis and can provide information on the bonding/coordination environment, valence electron density, and optoelectronic properties of a material. We collected dual EELS hyperspectral data sets, in which low-loss and high-loss spectra are collected at each pixel, of the Ba- and Sn-rich regions in several particles. Figure 4 shows one set of dual EELS spectra in which we again can see clear differences between the two regions indicated by the red and blue boxes. The core-loss data collected for energy losses in the range of 350−900 eV contains the Sn $M_{4,5}$ excitation at ∼485 eV and the Ba $M_{4,5}$ excitation at 781 and 796 eV (Figure 4c). The absence of Ba $M_{4,5}$ peaks in the Sn region (Figure 4c blue) confirms that the region indicated by the blue box in the HAADF image is predominantly Sn, whereas the red spectrum in Figure 4c shows the presence of both elements within the "porous" region of the HAADF image (red box). Additionally, we see a change in the fine structure of the Sn $M_{4,5}$ edge between the two data sets. From the Sn-rich region, the Sn $M_{4,5}$ edge is broad with a delayed maximum that is the typical fingerprint of other metals with full d-shells.[16,17] However, in the Ba-rich region, we see sharper features on the Sn $M_{4,5}$

https://doi.org/10.1021/acs.jpcc.1c02246
J. Phys. Chem. C 2021, 125, 15496−15502

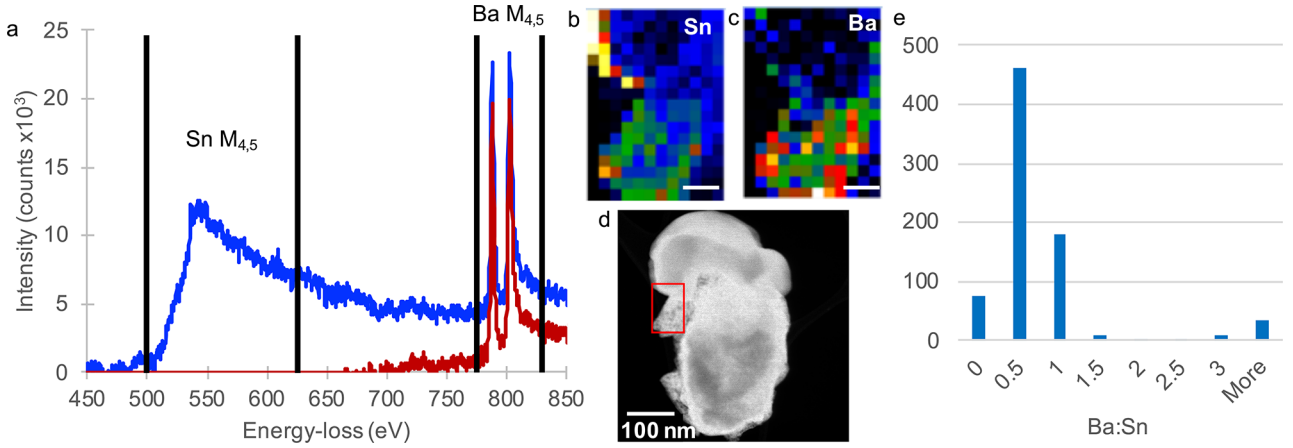

Figure 6. (a) Core-loss data after deconvolution of the Sn (blue) and Ba (red) ionization edges. The black lines indicate the energy windows used to create spectrum images in which each pixel contains only Sn (b) and Ba (c) signal. The scale bars in (b) and (c) are 25 nm. (d) HAADF image with the red box indicating the region from which the spectrum images were collected. (e) Frequency diagram showing the total Ba:Sn ratio per pixel.

onset, as well as additional fine structure following the maxima, indicating a change in the oxidation state of the Sn, consistent with Ba−Sn bonding. Importantly, the absence of any peaks associated with the oxygen K-edge excitation at 530 eV confirms that the sample has not been oxidized during the transfer to the TEM.

The low-loss region collected from 0−110 eV contains the Ba $O_{2,3}$ ionization edge at 15 eV and the Sn $N_{4,5}$ edge at 24 eV (Figure 4b). The plasmon peak, associated with the collective excitation of the valence electron density, is also present in this region. Each peak position is close in energy causing some overlap of the observed features. Therefore, further data processing is needed to draw more quantitative comparisons. In order to separate each contribution, a Kramers−Kronig (KK) analysis was performed in DigitalMicrograph (DM)[18] preceded by removal of the zero-loss peak (ZLP) and deconvolution using the Fourier-log method to remove the effects of plural scattering. The KK analysis allows for extraction of the real (ε_1) and imaginary (ε_2) parts of the complex dielectric function from the single scattering distribution of the inelastic spectrum (Figure 5).[16,17] In insulator or semiconductors, the onset of ε_2 can provide a measure of the band gap of a material. However, the onset can be influenced by both the ZLP removal and the energy resolution, which is defined by the full width at half maxima (FHWM) of the ZLP.[16,17] The removal of the ZLP was performed using the reflected tail method in DM with a half width at quarter maximum (HWQM) of 2. After various HQWM values were tested, a HWQM of 2 was chosen as any value greater than this resulted in artifacts in the data (Figure S1). Using these settings resulted in an ε_2 onset of ∼0.6 eV, indicating that improved energy resolution would be necessary to probe the band gap (0.2 eV) of $BaSn_2$. Finally, the optical refractive index is used to normalize the dielectric function in the KK analysis. Since this value is unknown for $BaSn_2$, we explored a range of refractive index values from 1.1 to 50 (Figure S2). A value of 2.7 was chosen as this is close to previously reported refractive index values of Sn.[19,20]

Figure 5c and d show the comparison of ε_1 and ε_2 for the Sn and Ba/Sn regions. Both the ε_1 and ε_2 plots show sharp intensity close to zero; however, these are artifacts associated with ZLP removal. In ε_2 (Figure 5d), the Sn $N_{4,5}$ edge at ∼24 eV is well-defined for both regions; however, the Ba $O_{2,3}$ edge at ∼15 eV is only visible in the data collected from the Ba/Sn region. The plasmon energy, which is dependent on the valence electron density, is identified as the minimum in the plot of ε_1.[16,17] Interestingly, this minimum is fairly consistent between the two regions at ∼14 eV (Figure 5c). The plasmon peak energy for β-Sn is 13.7 eV.[16] The peaks in ε_2 in the energy-loss range 4−8 eV may be associated with additional single electron transitions, but further investigation is needed to identify these excitations.

As mentioned previously, the core-loss data supports the presence of Sn and Ba_xSn_y regions, but to more quantitatively compare the two areas, a background subtraction and a deconvolution were performed for both the Sn and Ba ionization edges as described in the experimental section (Figure 6). From the deconvolved spectra, we created spectrum images in which each pixel contains only Sn or Ba signal by using an energy window over each ionization edge (Figure 6b and c). We then divided these images to get a Ba:Sn ratio per pixel for each data set. The ratios were plotted in a frequency diagram (Figure 6e) which shows an overall Ba:Sn ratio of 1:2 as the most common stoichiometry. These findings again support disproportionation of $BaSn_2$ into β-Sn and a Ba-rich Ba_xSn_y phase. The possible driving forces for this disproportionation include (i) a decrease in temperature, as was observed with the exposure to liquid nitrogen, (ii) oxidation, or (iii) exposure to a high-vacuum or a low-pressure environment. Our experimental results can eliminate the first two possibilities as the use of the environmental holder eliminated the need for transportation in liquid nitrogen, and the lack of an O K ionization edge (∼530 eV) in the core-loss data indicates successful air-free transfer. While complete oxidation of $BaSn_2$ may also lead to the formation of β-Sn, powder XRD data collected on $BaSn_2$ powder before and after exposure to ppm-level oxygen from the glovebox for 6 days does not show the formation of β-Sn, indicating that ppm-level oxygen is not enough to drive disproportionation (Figure S3). Therefore, the only difference between the material analyzed by XRD and S/TEM is the exposure to the high-vacuum atmosphere in the microscope. To test whether the low-pressure environment is the potential driving force for disproportionation, we collected XRD data of $BaSn_2$ particles

https://doi.org/10.1021/acs.jpcc.1c02246
J. Phys. Chem. C 2021, 125, 15496−15502

before and after exposure to a vacuum of 1.4×10^{-4} mbar for 18 h. The XRD data in Figure 7 shows the presence of β-Sn in

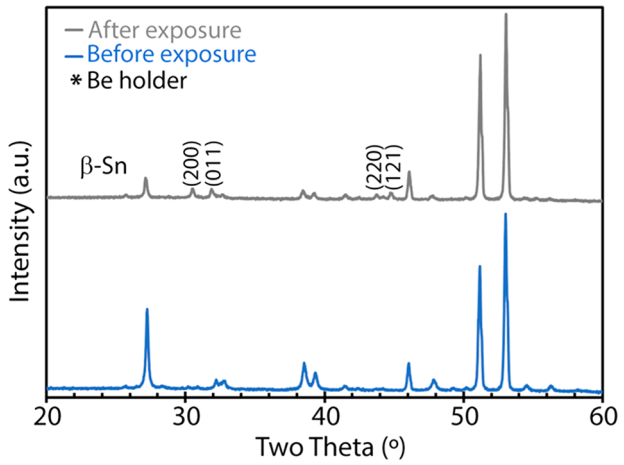

Figure 7. XRD of $BaSn_2$ particles before (blue) and after (gray) exposure to 10^{-4} mbar vacuum for 18 h. The new reflections are indicative of β-Sn formation.

the postvacuum spectrum. While there is agreement between the XRD and S/TEM analyses, there are also a few important differences. The XRD data in Figure 7 suggests that a small amount of β-Sn is formed when the material is exposed to a high vacuum and that the remaining material is still primarily $BaSn_2$. In contrast, the S/TEM data suggests the formation of significant amounts of β-Sn, and the remaining Ba-rich material has a variable stoichiometry. While our results clearly show that the exposure to a low-pressure environment initiates the disproportionation of $BaSn_2$, in the TEM the extent of the disproportionation may be greater due to the higher vacuum and/or greater exposed surface area of the particles.

CONCLUSION

In conclusion, we have shown that $BaSn_2$ disproportionates into β-Sn and a Ba-rich Ba_xSn_y phase under the influence of low pressure. XRD data indicates that the starting material is primarily $BaSn_2$ with traces of $BaSn_3$. S/TEM characterization via HRTEM and HAADF imaging, EDS, and EELS analysis was used to show a correlation between morphology, composition, and crystallinity of the Sn and Ba-rich regions. Sn-rich areas show a homogeneous morphology in the HAADF images and have long-range ordering with SAED patterns that are consistent with β-Sn. Porous regions in the HAADF image have a varying Ba:Sn ratio and are primarily amorphous or polycrystalline. Whole particles on average exhibit a Ba:Sn ratio of 1:2 as indicated by both EDS and EELS analysis. XRD analysis shows the formation of β-Sn after exposure to a low-pressure environment. The use of an environmental vacuum transfer TEM holder enabled the elimination of temperature and oxidation as alternative driving forces for the disproportionation.

ASSOCIATED CONTENT

Supporting Information

The Supporting Information is available free of charge at https://pubs.acs.org/doi/10.1021/acs.jpcc.1c02246.

Figures of the ZLP removal Kramers−Kronig analysis and XRD of $BaSn_2$ exposed to ppm-level oxygen for 6 days (PDF)

AUTHOR INFORMATION

Corresponding Author

David W. McComb − *Center for Electron Microscopy and Analysis and Department of Materials Science and Engineering, The Ohio State University, Columbus, Ohio 43210, United States*; Email: mccomb.29@osu.edu

Authors

Amanda H. Trout − *Center for Electron Microscopy and Analysis and Department of Materials Science and Engineering, The Ohio State University, Columbus, Ohio 43210, United States*; orcid.org/0000-0001-9204-8068

Kelsey L. Hodge − *Department of Chemistry and Biochemistry, The Ohio State University, Columbus, Ohio 43210, United States*

Michael Scudder − *Department of Chemistry and Biochemistry, The Ohio State University, Columbus, Ohio 43210, United States*

Joshua E. Goldberger − *Department of Chemistry and Biochemistry, The Ohio State University, Columbus, Ohio 43210, United States*; orcid.org/0000-0003-4284-604X

Complete contact information is available at: https://pubs.acs.org/10.1021/acs.jpcc.1c02246

Notes

The authors declare no competing financial interest.

ACKNOWLEDGMENTS

This work was supported by the Center for Emergent Materials, an NSF-funded MRSEC under Award No. DMR-1420451. We acknowledge partial support from the Center for Emergent Materials: an NSF MRSEC under award number DMR-2011876.

REFERENCES

(1) Vogt, P.; De Padova, P.; Quaresima, C.; Avila, J.; Frantzeskakis, E.; Asensio, M. C.; Resta, A.; Ealet, B.; Le Lay, G. Silicene: Compelling Experimental Evidence for Graphenelike Two-dimensional Silicon. *Phys. Rev. Lett.* **2012**, *108*, 155501.

(2) Dávila, M. E.; Le Lay, G. Few Layer Epitaxial Germanene: A Novel Two-Dimensional Dirac Material. *Sci. Rep.* **2016**, *6*, 1−9.

(3) Liao, M.; Zang, Y.; Guan, Z.; Li, H.; Gong, Y.; Zhu, K.; Hu, X.; Zhang, D.; Xu, Y.; Wang, Y.; et al. Superconductivity in Few-Layer Stanene. *Nat. Phys.* **2018**, *14*, 344−348.

(4) Zhu, F.; Chen, W.; Xu, Y.; Gao, C.; Guan, D.; Liu, C.; Qian, D.; Zhang, S.; Jia, J. Epitaxial Growth of Two-Dimensional Stanene. *Nat. Mater.* **2015**, *14*, 1020−1026.

(5) Ezawa, M. Monolayer Topological Insulators: Silicene, Germanene, and Stanene. *J. Phys. Soc. Jpn.* **2015**, *84*, 121003.

(6) Molle, A.; Goldberger, J. E.; Houssa, M.; Xu, Y.; Zhang, S.; Akinwande, D. Buckled Two-Dimensional Xene Sheets. *Nat. Mater.* **2017**, *16*, 163−169.

(7) Bianco, E.; Butler, S.; Jiang, S.; Restrepo, O. D.; Windl, W.; Goldberger, J. E. Stability and Exfoliation of Germanane: A Germanium Graphane Analogue. *ACS Nano* **2013**, *7*, 4414−4421.

(8) Huey, W. L. B.; Goldberger, J. E. Covalent Functionalization of Two-Dimensional Group 14 Graphane Analogues. *Chem. Soc. Rev.* **2018**, *47*, 6201.

(9) Arguilla, M. Q.; Cultrara, N. D.; Scudder, M. R.; Jiang, S.; Ross, R. D.; Goldberger, J. E. Optical Properties and Raman-Active Phonon

Modes of Two-Dimensional Honeycomb Zintl Phases. *J. Mater. Chem. C* **2017**, *5*, 11259−11266.
(10) Young, S. M.; Manni, S.; Shao, J.; Canfield, P. C.; Kolmogorov, A. N. $BaSn_2$: A Wide-Gap Strong Topological Insulator. *Phys. Rev. B: Condens. Matter Mater. Phys.* **2017**, *95*, 85116.
(11) Huang, H.; Liu, J.; Vanderbilt, D.; Duan, W. Topological Nodal-Line Semimetals in Alkaline-Earth Stannides, Germanides, and Silicides. *Phys. Rev. B: Condens. Matter Mater. Phys.* **2016**, *93*, 201114.
(12) Guo, S.; Qiu, L. Thermoelectric Properties of Topological Insulator $BaSn_2$. *J. Phys. D: Appl. Phys.* **2017**, *50*, 015101.
(13) Kim, S.; Fässler, T. F. Crystal Structure of Barium Distannide, BaSn2. *Z. Kristallogr. - New Cryst. Struct.* **2008**, *223*, 325−376.
(14) Lichtenstein, T.; Gesualdi, J.; Yu, C.; Kim, H. Thermochemical Properties and Phase Transitions of Ba-Sn Alloys from Thermal Characterization and emf Measurements. *J. Alloys Compd.* **2019**, *811*, 151531.
(15) Ropp, R. C. Chapter 5: Group 14 (C, Si, Ge, Sn, and Pb) Alkaline Earth Compounds. In *Encyclopedia of the Alkaline Earth Compounds*; Elsevier: Amsterdam, Netherlands, 2013; pp 351−480.
(16) Egerton, R. F. *Electron Energy-Loss Spectroscopy in the Electron Microscope*; Springer: New York, 2011.
(17) Daniels, J.; Festenberg, C. v.; Raether, H.; Zeppenfeld, K. Optical Constants of Solids by Electron Spectroscopy. In *Springer Tracts in Modern Physics*; Höhler, G., Ed.; Springer Tracts in Modern Physics; Springer: Berlin, Heidelberg, 1970; Vol. *54*.
(18) *Digital Micrograph, version 3.4; User's Guide*; Gatan Inc.: Warrendale, PA, 1999.
(19) Golovashkin, A. I.; Mogilevich, G. P. Optical and Electrical Properties of Tin. *J. Exp. Theor. Phys.* **1964**, *19*, 310−317.
(20) Takeuchi, K.; Adachi, S. Optical Properties of Beta-Sn Films. *J. Appl. Phys.* **2009**, *105*, 073520.

https://doi.org/10.1021/acs.jpcc.1c02246
J. Phys. Chem. C 2021, 125, 15496−15502